High performance quasi-solid-state supercapacitors with peanut-shell-derived porous carbon

Neetu Yadav, Manoj K. Singh, Nitish Yadav, S.A. Hashmi*

Department of Physics & Astrophysics, University of Delhi, Delhi, 110007, India

HIGHLIGHTS

- AC powder is synthesized from bio-waste peanut-shells by two different routes.
- Ethanol-soaked peanut-shell-derived AC (EPAC) shows high meso-porosity.
- EPAC electrodes show specific capacitance of $\sim 189\,F\,g^{-1}$ in solid-state-EDLCs.
- EDLC is stable for $\sim 10^4$ cycles with $\sim 28\%$ fading and 100% Coulombic efficiency.
- Capacitor offers specific energy 26 Wh kg^{-1} and specific power 57 kW kg^{-1}.

GRAPHICAL ABSTRACT
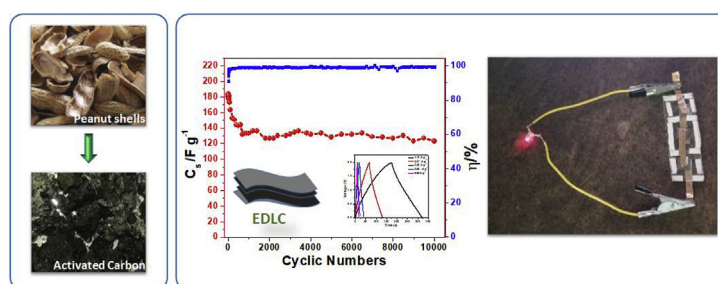
ABSTRACT

We present high performance symmetric quasi-solid-state electrical double layer capacitors (EDLCs) with activated carbon (AC) electrodes produced from peanut-shells. Two different (ethanol soaking and hydrothermal) pre-treatments were given to peanut-shells to tailor ACs' microstructure and comparative supercapacitive performance have been evaluated with Mg-salt (magnesium trifluoromethanesulfonate, Mg (Tf)$_2$) and ionic liquid, IL (1-ethyl-3-methylimidazolium-trifluoromethanesulfonate, EMITf) incorporated gel polymer electrolytes (GPEs). Morphological and porosity studies indicate larger content of mesoporous interiors in ACs obtained from ethanol pre-soaking, offering superior capacitive performance over hydrothermally-treated ACs. The high room temperature ionic conductivity ($\sim 3.8 \times 10^{-3}\,S\,cm^{-1}$), good electrochemical stability window ($\sim 3.7\,V$) and flexible nature of the free-standing films of GPEs Mg (Tf)$_2$/IL/poly (vinylidinefluoride-*co*-hexafluoropropylene) (PVdF-HFP) show their excellent compatibility with AC-electrodes. Electrochemical impedance spectroscopy and cyclic voltammetry indicate high-rate capability of the device. The AC-electrodes, prepared via ethanol-soaking offer superior performance during charge-discharge tests in terms of specific capacitance ($\sim 189\,F\,g^{-1}$), energy ($\sim 26\,Wh\,kg^{-1}$) and maximum power ($\sim 57\,kW\,kg^{-1}$) with Mg-salt/IL incorporated GPE-film as compared to the devices with only IL-based GPE-film. The EDLC shows stable performance up to $\sim 10,000$ charge-discharge cycles with $\sim 28\%$ initial fading in specific capacitance. The EDLC is thermally stable in the temperature range from -50 to $70\,°C$.

1. Introduction

Over the last few decades, market for the portable electronic devices

and electrical vehicles with hybrid power system is growing rapidly, for which, there is an urgent need of efficient energy-storage devices like rechargeable ion-batteries and supercapacitors [1,2]. Significant

---

research and development is globally ongoing on electric double layer capacitors (EDLCs), which is an important and most reported class of supercapacitors. They have attracted world-wide attention due to their high power delivering ability and excellent charge-discharge cycling performance [2]. High surface area porous carbons including activated carbon, carbon aerogels, carbon nanotubes (CNTs), carbon nanofibers (CNFs), graphene, etc. are important electrode materials for EDLCs [3–8]. In this race, the activated carbons are still potential candidates, which are prepared from various organic compounds such as poly acrylonitrile (PAN) [9], coal-tar pitch [10], carbides [11], etc. However, the production processes of activated carbon from these compounds are hazardous and costly.

In order to develop 'green' energy storage systems like EDLCs and to make them cost-effective, waste biomass materials are reported to be used to produce activated porous carbon for EDLC electrodes. Biomass-based activated carbons can be produced from a variety of sources namely coconut shell [12,13], coffee shell [14], almond shell [15], tea-leaves [16], rice husk, poplar wood [17], etc. and are reported to develop high performance EDLCs. Recently, peanut-derived carbon is reported in various energy storage applications namely EDLCs [18], sodium-ion batteries and capacitors [19] etc. The peanut-shell based activated carbons offer high surface area ($\sim 2100\, m^2\, g^{-1}$), graphene-like flakes etc., suitable for efficient EDLC-electrodes, while being environment friendly and cost-effective at the same time. It may be noted that peanut industry generates considerable quantities of shells (~ 6 million tons) each year, which are entirely discarded as bio-waste.

Peanut-shell is ligno-cellulosic material, containing cellulose macro-fibril bundles, made of a number of micro-fibrils. Each micro-fibril is a crystalline, longitudinal arrangement of cellulose sheets parallel to each other. These sheets are further made of longitudinally arranged chains of cellulose. The crystalline fibrils are the packing of a number of flat sheets made of uniformly arranged cellulose chains, bonded with each other by van der Waal's forces [20]. Lignin and hemi-cellulose are present in the space between macro-fibrils and give the overall structural strength to the fiber. The content of cellulose, lignin, and hemi-celluloses in peanut-shell is 34–45%, 27–33% and 12–16% (w/w), respectively [21,22]. It may be noted that different processes of pretreatments, before carbonization and activation, affect the above-mentioned components of peanut-shells in different ways, so, different porous textures of the activated carbon are obtained.

In general, the high surface area activated carbon has the ability to store large amount of charges, however, mostly nonlinear relationship has been observed between the capacitance shown by the material and its specific surface area [23]. This is due to the possibility that not all the pores of the electrodes are necessarily accessible to the electrolyte ions. Generally, micro- and mesopores of carbon electrodes, which greatly affect the performance of the EDLCs, are controlled by the activation processes [24,25]. Various activation processes such as physical, chemical, or a combination of both are described in literature [15,26]. The carbon materials are generally activated chemically followed by physical activation to modify their various properties such as porosity, microstructure and surface area. For the chemical activation, different activating agents are employed, namely: H_3PO_4, $ZnSO_4$, $ZnCl_2$, K_2CO_3, Na_2CO_3, NaOH, KOH, $CaCl_2$, etc. [15,26]. Recently, Satlewal et al. reported that soaking of biomass in ethanol for longer duration before chemical and physical activation processes is an important approach to observe improved performance of carbon electrodes [27].

EDLCs of latest generation employ, in general, quasi-solid-state films of gel polymer electrolytes (GPEs) instead of liquid electrolytes. GPEs comprise liquid electrolyte (e.g. aqueous H_2SO_4, KOH, etc. or salts dissolved in organic solvents, or ionic liquids or their mixture with salts) entrapped in host polymers e.g. PVdF-HFP, PMMA, PEO, PVA, etc. EDLCs/supercapacitors based on liquid electrolytes mostly suffer from various common drawbacks such as leakage, corrosion, self-discharge, etc. On the other hand, GPEs have proven to be potential separators/electrolytes due to many advantageous reasons such as

flexibility, mouldability, and high ionic conductivity, almost comparable to liquid electrolytes. Particularly, ionic liquid-based GPEs offer excellent thermal and electrochemical stability, in addition to the other advantageous properties, mentioned above [28,29]. From safety point of view also, ionic liquid based GPEs are attractive due to non-volatile and non-flammable nature of ionic liquids. GPEs, employing organic solvents or ionic liquids, used for EDLC applications, mostly contain Li-salts [30]. The Mg-salts (e.g. magnesium trifluoromethane sulfonate, Mg (Tf)$_2$, magnesium bis(trifluoromethan sulfonyl)imide, Mg (TFSI)$_2$, Mg(ClO$_4$)$_2$, etc.), on the other hand, may be a better substitute to incorporate in GPEs, as Mg-ions are doubly charged cations with ionic sizes comparable to Li-ions. Few recent studies indicate that GPEs containing Mg-salts are equally suitable for supercapacitor-like applications [31,32].

In this paper, a comparative performance study has been presented on EDLCs, fabricated with peanut-shell derived activated carbon electrodes (prepared by two processes) and ionic liquid incorporated Mg^{2+}-ion conducting GPE film. To prepare activated carbons, raw peanut-shell powder was treated by two different processes i.e. soaking in ethanol for long duration and hydrothermal treatment, before their chemical and physical activations. These two pretreatments have different impacts on the nanoscale structure, which ultimately define the content and quality of meso- and micropores in the carbon, which greatly influence the performance characteristics of EDLCs. The GPE, employed as flexible electrolyte, comprised of 0.3 M solution of magnesium triflate (Mg (Tf)$_2$) in ionic liquid 1-ethyl-3-methylimidazolium trifluoromethane-sulfonate (EMITf), entrapped in a host polymer poly (vinylidene fluoride-co-hexafluoropropylene (PVdF-HFP). The characteristics of EDLCs have been studied based on electrochemical impedance spectroscopy (EIS), cyclic voltammetry (CV) and galvanostatic charge-discharge techniques over numerous cycles. Role of porosity in carbon-electrodes and effect of Mg-salt in gel electrolyte in the performance of EDLCs has been specifically discussed.

2. Experimental

2.1. Materials

Ethanol (C$_2$H$_5$OH; AR grade) and zinc chloride (ZnCl$_2$; purity $\sim 95\%$) were procured from Merck Chemicals. Acetylene black (AB), co-polymer poly (vinylidinefluoride-co-hexafluoro-propylene) (PVdF-HFP), magnesium trifluoromethanesulfonate (Mg (Tf)$_2$), and ionic liquid (IL) 1-ethyl-3-methylimidazolium trifluoromethanesulfonate (EMITf) were procured from Sigma-Aldrich. All the chemicals were used without further purification. The un-roasted peanuts (with shells) were purchased from a local market.

2.2. Preparation and characterization of porous activated carbon

Peanut shells were washed with de-ionized water, and vacuum dried at $\sim 110\,°C$, for 12 h before use. The porous activated carbon was prepared following two procedures where the peanut shells were given two different treatments before their chemical and physical activations. The preparation processes of activated carbons are schematically represented by Fig. 1. The pre-treatments were either soaking in ethanol, or a hydrothermal treatment. In the first process, peanut shells were soaked with ethanol for 30 days and then dried in vacuum oven at $\sim 110\,°C$ for 14 h. Thereafter, the material was crushed into powder form using mortar and pestle for chemical and physical activation. The powder was then mixed in 20 ml deionised water with activation agent ZnCl$_2$ in the ratio of 1:2 w/w. The mixture was then stirred thoroughly followed by drying it overnight at $\sim 110\,°C$ [12]. The material was then placed into a tube furnace and heated up to $\sim 800\,°C$ with heating rate $\sim 5\,°C$ per min under constant flow of nitrogen for chemical activation. This process was followed by CO$_2$ flow for 2 h for its physical activation. After natural cooling to room temperature, the resulting material was
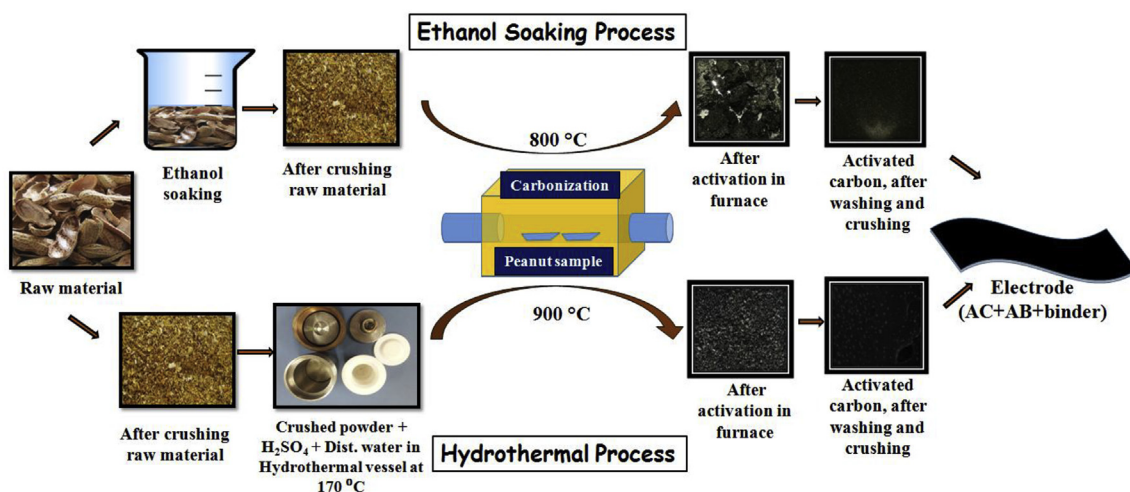
Fig. 1. Schemes for preparation of activated carbon using ethanol-soaking and hydrothermal pre-treatments.

washed with dilute HCl solution to remove the zinc ions. The material was further washed by hot distilled water to remove chloride ions. Finally, the carbon material (named EPAC) was dried in vacuum oven overnight at ~110 °C and crushed to powder form. The mass of the activated carbon electrode on the graphite sheets was ~0.88 mg cm^{-2}.

The second process, namely hydrothermal pre-treatment followed by activation is given as follows. 1.5 g peanut-shell powder and 3 ml H$_2$SO$_4$ were mixed in 20 ml of distilled water and stirred for ~6 h. The mixture was sealed in teflon-lined stainless steel autoclave vessel of 50 ml capacity [33]. The vessel was kept in a muffle furnace at ~170 °C for ~72 h and then allowed to cool naturally to room temperature. The resulting material was in the form of biochar, which was separated from the liquid part by vacuum filtration. The material was washed with hot distilled water until its pH reached a value of ~7, and then dried in vacuum oven at ~110 °C overnight. For the physical and chemical activations, the same procedure was followed, as mentioned above for EPAC material. The activated carbon electrode material obtained via this process is referred to as HPAC.

The porous activated carbons (EPAC and HAPC) were characterized by field-emission scanning electron microscopy (FESEM) using TESCAN Instrument MIRA3 LMH (Czech Republic) at a potential difference of 20 kV. The specific surface area and porosity analysis was carried out by N$_2$-adsorption-desorption (at 77 K) in a Micromeritics, U.S.A. (Gemini-V) surface area and pore size analyzer. X-ray measurements were performed on an X-ray diffractometer (D8, Brucker, U.S.A.) using Cu-Kα radiation (λ ~1.5406 Å) at a scan rate of 2° per minute. A Renishaw Invia Raman spectrometer (U.K.), equipped with a charge-coupled device (CCD) detector, was employed for Raman measurements. An Ar-ion laser with a 514.5 nm wavelength and a spot diameter of 1–2 μm was used to excite the samples.

2.3. Preparation and characterization of gel polymer electrolytes

The gel polymer electrolytes (GPEs) were prepared by "solution-cast" technique, which involves dissolving the host polymer matrix (PVdF-HFP) in a suitable solvent acetone and then adding pure IL or 0.3 M solution of Mg (Tf)$_2$ in IL in this solution. Initially, 1 g of PVdF-HFP was dissolved in about 20 ml of acetone and then 4 g of IL (EMITf) or Mg (Tf)$_2$/IL solution was added. The final solutions were stirred on magnetic stirrer for 5–6 h at room temperature (~27 °C) and poured in glass petri-dishes, where the volatile solvent (acetone) was allowed to evaporate slowly. Finally, the free-standing and flexible GPEs films were obtained, as pictorially shown in Fig. 2(A). The two compositions of GPEs are referred to as follows:

(i) GPE-1: EMITf/PVdF-HPF (80:20w/w),
(ii) GPE-2: 0.3 M Mg (Tf)$_2$ solution in EMITf/PVdF-HPF(80:20w/w).

The electrochemical performances of the GPE film were tested by measuring ionic conductivity and electrochemical stability window (ESW) using an electrochemical workstation (CHI660E, CH Instruments, USA). The temperature dependence of ionic conductivity of GPEs was recorded on a Broadband Dielectric/Impedance Analyzer (C-50 Alpha A, Novocontrole, Germany).

2.4. Fabrication and characterization of EDLCs

For the fabrication of quasi-solid-state electric double layer capacitors, the electrodes were prepared by mixing activated carbons (EPAC or HPAC), acetylene black (conducting agent) and PVdF-HFP (binder) in a common organic solvent acetone in the weight ratio of 80:10:10 and homogenous slurry was obtained. Thereafter, the slurry was spin coated on flexible graphite sheets (250 μm thick, Nickunj Eximp Entp. India) of area of 1 × 1 cm^2. The coated graphite sheets were dried overnight at ~100 °C.

Each EDLC cell was fabricated by drop-casting dilute solution of GPE compositions on two carbon-coated electrodes followed by thoroughly drying at room temperature. Two such systems are placed over each other such that the GPE coated sides stay together, giving a sandwich geometry of AC|GPE|AC as shown in Fig. 2(B). The thickness of GPE film in the cell was maintained at ~400 μm. Thus, four EDLC cells were fabricated using two types of activated carbon electrodes and two types of GPEs with the following configurations:

Cell#1: HPAC | GPE-1 | HPAC
Cell#2: EPAC | GPE-1 | EPAC
Cell#3: HPAC | GPE-2 | HPAC
Cell#4: EPAC | GPE-2 | EPAC

The systems where placed in split test cell (Model: EQ -3ESTC, MTI Corporation, USA) for measurements. A photograph the cell is given in supplementary information (Fig.S5). The performance characteristics of the EDLC cells were evaluated using electrochemical impedance spectroscopy (EIS), cyclic voltammetry (CV) and galvanostatic-charge-discharge (GCD) technique. The same electrochemical analyzer as mentioned above recorded the EIS and CV patterns. The GCD studies were performed using a charge–discharge unit (BT-2000, Arbin Instruments, USA).
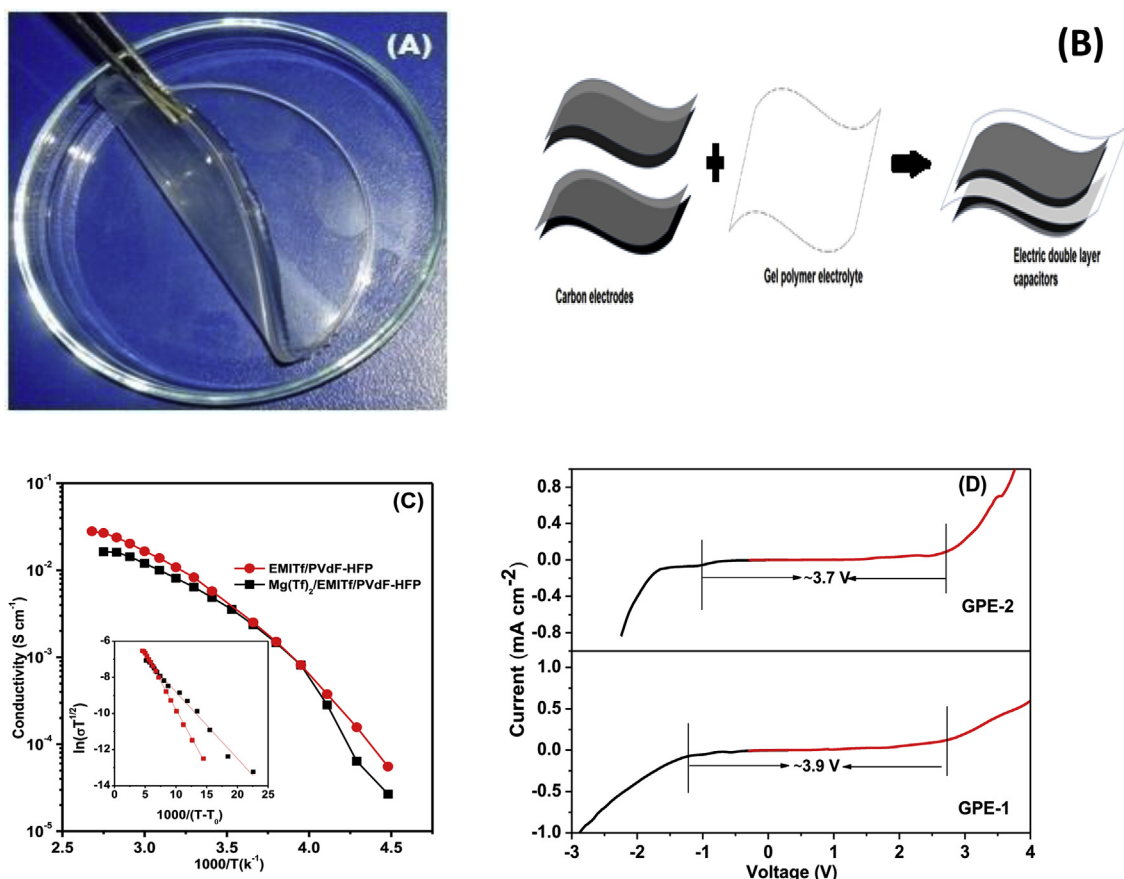
Fig. 2. (A) Photograph of gel polymer electrolyte showing the flexible nature, (B) Schematic representation of the fabrication of an EDLC assembly with gel polymer electrolyte, (C) σ vs. 1/T plots of EMITf/PVdF-HFP blend and Mg (Tf)$_2$/EMITf/PVdF-HFP gel polymer electrolyte (inset shows the fitted curves using VTF-equation), (D) Electrochemical stability window for EMITf/PVdF-HFP (GPE-1) and Mg (Tf)$_2$/EMITf/PVdF-HFP (GPE-2) gel polymer electrolytes.

3. Results and discussion

3.1. Electrochemical properties of GPEs

The GPE films possess excellent mechanical, thermal and electrochemical stabilities with room temperature ionic conductivity of the order of $10^{-3}\,\mathrm{S\,cm^{-1}}$. The physical and thermal characterizations of GPE-1 and GPE-2 have been performed previously by us [34]. The extended electrochemical properties have been discussed in the present study. The room temperature ionic conductivity of GPE-1 (IL/Polymer) has been observed to be $\sim 4.6 \times 10^{-3}\,\mathrm{S\,cm^{-1}}$, which is comparable to that of pure IL (EMITf) and has the additional property of appreciable dimensional stability. On the addition of magnesium salt to EMITf/PVdF-HFP gel, a slight decrease in conductivity ($\sim 3.8 \times 10^{-3}\,\mathrm{S\,cm^{-1}}$) has been observed, which is due to the increase in viscosity of the liquid phase on the addition of the magnesium salt [34]. The temperature dependent ionic conductivity (i.e. σ versus 1/T plots) of GPE-1 and GPE-2, as depicted in Fig. 2(C), show the curved variation indicating Vogel-Tamman-Fulcher (VTF) type behavior, expressed by the following equation:

$$\sigma = AT^{-1/2}exp\left(-\frac{B}{T - T_o}\right) \tag{1}$$

where parameter A is pre-exponential factor indicating the conductivity at infinitely high temperature, parameter B is pseudo-activation energy which is associated with the rate at which viscosity changes with temperature and T_o is the pseudo-glass transition temperature. These fitting parameters (A, B, and T_o) have been estimated using nonlinear least square (NLLS) fitting of the experimental data and listed in

Table 1
Fitting parameters of conductivity versus temperature data using VTF equation.

Sample code	Compositions	A (S cm^{-1} K$^{1/2}$)	B (K)	T$_o$ (K)	Fragility Index
GPE-1	EMITf/PVdF-HFP	2.63	383.21	183	0.48
GPE-2	Mg (Tf)$_2$/EMITf/ PVdF-HFP	8.71	581.94	162	0.27

Table 1. The fitted parameters exhibit an excellent agreement with experimental data with regression value of $R^2 \geq 0.99$. Another important parameter associated with visco-elastic property of the GPEs that can be evaluated from these VTF fitting parameters is the fragility index (F), which can be estimated from the expression $F = T_o/B$ [35]. The reciprocal of the fragility index is referred to as the strength parameter (D) [36]. The fragility index for both the polymer electrolyte systems is mentioned in Table 1. A comparison indicates that the strength of the GPE film improves when the Mg (Tf)$_2$ salt is incorporated in the binary system PVdF-HFP/EMITf (Table 1). This is also reflected in σ vs 1/T plots (Fig. 2(C)). The electrolyte GPE-1 (EMITf/PVdF-HFP) is found to be less curved as compared to that of the Mg (Tf)$_2$ incorporated electrolyte GPE-2.

The electrochemical stability window (ESW) i.e. working voltage range for the electrolytes GPE-1 and GPE-2 has been evaluated by linear sweep voltammetry (LSV). The cell configuration used for LSV is GC|GPEs|Ag, in which the glassy carbon (GC) sheet is used as working electrode and silver (Ag) foil as both the quasi-reference and counter electrodes. The electrochemical stability window has been observed to be approximately same in the anodic region ($\sim 2.7\,\mathrm{V}$) for both the

electrolytes, while it is slightly reduced in the cathodic region from -1.2 to -1.0 V on the addition of magnesium salt (Fig. 2(D)). This could be because the anions ($TFSI^-$) are common in both the ionic liquid as well as Mg-salt, so, they are getting oxidized in the anodic region at the same potential for both the GPEs (with and without Mg-salt). On the other hand, the cations Mg^{2+} are reduced at slightly lower potential (for GPE-2 with Mg-salt) as compared to that of EMI^+ ions in the case of GPE-1 (without Mg-salt) in the cathodic region. Another cause could be the possible interaction of Mg^{2+} ions with imidazolium cations [37] while approaching simultaneously towards GC-cathode, and the resulting complex having lower cathodic stability. Overall, the ESW is ~ 3.9 V and ~ 3.7 V vs. Ag for GPE-1 and GPE-2, respectively. These stability ranges are sufficient for their deployment in EDLCs and other electrochemical devices.

3.2. Characteristics of activated carbon

The FESEM images of both types of porous activated carbons (EPAC and HPAC) are shown in Fig. 2. Distinct difference has been observed in the images of the EPAC and HPAC materials. The HPAC powder is flaky in appearance while the EPAC is seen to be granular as shown in FESEM images, recorded at the 5 μm scale (Fig. 3(A) and C). Also, most of the material in HPAC resides in the bulk while in EPAC the smaller granules expose most of the carbon materials to the atmosphere. At higher magnifications (Fig. 3(B) and D), nanosized pores are observed in both the materials. However, these pores are found with lower density in HPAC as compared to that of EPAC.

The quantitative estimation of surface area and other porosity parameters has been performed by recording N_2-adsorption-desorption isotherms of porous activated carbons (EPAC and HPAC) at 77 K, as depicted in Fig. 4(A). A considerable difference in the isotherms of EPAC and HPAC powders has been observed. According to IUPAC classification, HPAC powder shows Type-I isotherm, while EPAC powder shows the Type-IV isotherms [38–40]. The initial steep rising behavior of both the isotherms for EPAC and HPAC indicates the major uptake of nitrogen at low relative pressure corresponding to the single layer sorption in different types of pores. Furthermore, the gradual increase in the isotherm with respect to the relative pressure and the presence of hysteresis loop during N_2-desorption indicate the presence

of mesoporous interiors in EPAC powder (Fig. 4(A)). Various parameters like BET surface area, total pore volume, micropore area, micro- and mesopore volumes, and average pore size of the two materials are listed in Table 2. The total pore volume was estimated at the relative pressure of ~ 0.95 and found that its value is higher for EPAC as compared to HPAC. The micropore area and volume were estimated from t-plots [41]. The mesopore volume has been calculated by subtracting the micropore volume from the total pore volume.

Hysteresis loops are not observed in Type-I isotherms of carbon materials, as clearly seen in the case of HPAC powder (Fig. 4(A)). The Type-IV isotherms show several types of hysteresis loops [39]. The hysteresis loop of EPAC is categorized as H4-type (Fig. 4(A)), the area of which gives the indication of the ratio of mesopore to micropore volume as the hysteresis is mainly due to remaining adsorbed N_2 molecules in the mesopores. The ethanol soaked peanut shells based activated carbon (EPAC) shows enhanced mesopore volume, indeed, the mesopore volume of EPAC is ~ 2.5 times higher than that of HPAC (Table 2). Ethanol has been reported to be a good solvent to remove lignin and hemicelluloses. Aqueous ethanol has ability to remove lignin and hemicellulose efficiently due to its ability to penetrate deep and uniformly in the wood structure at elevated temperature [42–44]. In the present case, as mentioned earlier, the peanut shells were soaked in excess ethanol solution for a period of one month. For such a long duration at room temperature and without any acidic or basic additives to the ethanol, we expect the ethanol to slowly dissolve and remove the lignin and hemicellulose of the peanut shells without much affecting the arrangement of the crystalline cellulose microfibrils. This will lead to an arrangement of cellulose fibrils without any lignin or hemicellulose between them. Each microfibril is 10–30 nm in diameter, which gives an empty space of approximate size 2–6 nm between these microfibrils. During activation, $ZnCl_2$ and CO_2 can easily penetrate these spaces and lead to increase in their diameter [33]. Also, the crystalline cellulose regions around these mesopores, upon carbonization, become more or less graphitic, and hence increase the electron conducting nature of the activated carbon.

In the case of HPAC, hydrothermal pretreatment with a strong acid leads to hydrolysis and dissolution of non-crystalline components like hemicellulose and lignin. The cellulose microfibrils are also spliced, loosened, disrupted and swelled at the rigorous experimental conditions (at 170 °C for 72 h in sealed vessel) [33]. Additionally, the acid treatment adds functional groups on the cellulose chains. At the same time, some carbonization of the cellulose chains in the microfibrils happens during this high temperature pretreatment, which leads to preservation of the graphitic architecture of cellulose, but with large interlayer spacing. The large number of micropores in HPAC are expected to arise out of the disruption caused in the crystalline structure of the cellulose. The smaller crystalline domains and larger interlayer spacing of HPAC are evident from XRD analysis, discussed below.

This difference in the mesoporous interiors affects the performance of the EDLC cells and is discussed later. The pore size distribution of the activated carbons has been calculated using the desorption data of isotherms following the Barrett-Joyner-Halenda (BJH) method and depicted in Fig. 4(B). The pore size distribution shows a relatively sharp peak, centered at ~ 2.3 nm for HPAC material, whereas, the EPAC powder shows a broad feature having predominant pore size range from 2.2 to 3.5 nm with gradual decrease up to ~ 15 nm. This indicates that pre-soaking of ethanol in peanut shells converted the micropores to wide range of mesopores and increased the total pore volume (Table 2).

Fig. 4(C) shows XRD patterns of the EPAC and HPAC powders, which consist of two broad peaks for each material. The peaks for EPAC material lie between 15° and 35°, and 40° and 50° corresponding to (002) and (100) planes, respectively. For HPAC, the (002) peak is relatively broader, observed between 10° and 35°. A shift of ~ 3.5° in the XRD peak corresponding to (002) planes of HPAC has been observed towards left with respect to that of EPAC powder. This shift indicates an increase in interplanar spacing between the graphitic layers of HPAC.
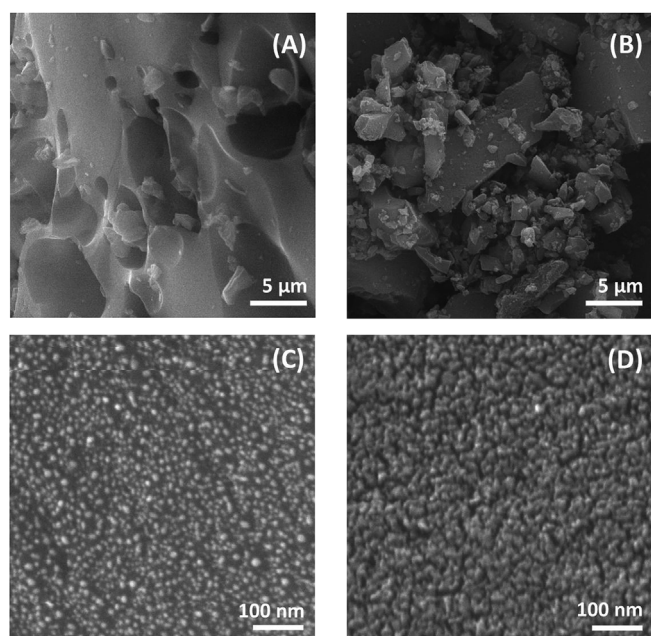

Fig. 3. FESEM images of (A, C) HPAC magnification at 5.0 k × and 225 k × and (B, D) EPAC at 5.0 k × and 225 k × .
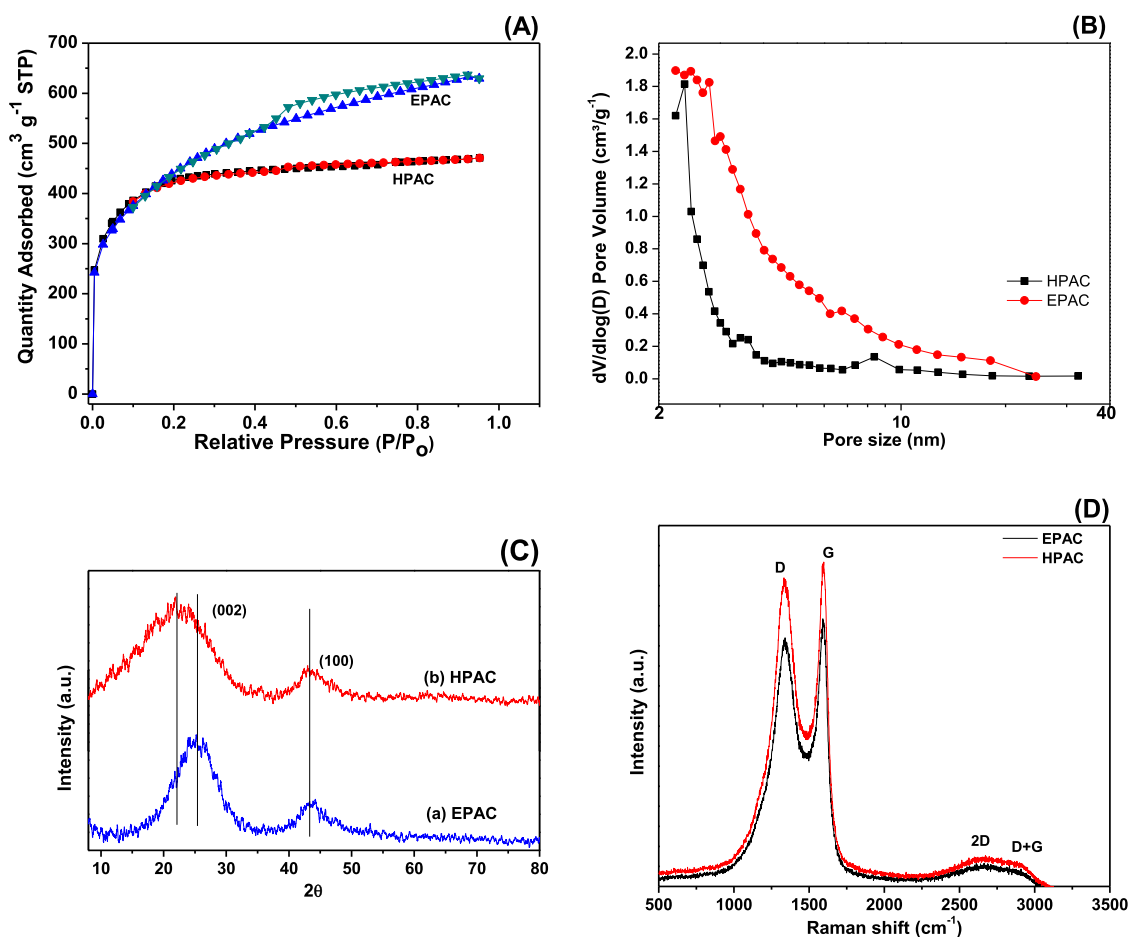
Fig. 4. (A) N_2 adsorption-desorption isotherms at 77 K, (B) Pore size distribution, (C) X-ray diffraction patterns, and (D) Raman spectra of HPAC and EPAC.

Table 2
BET specific surface area and porosity parameters of Peanut-shell-derived activated carbons.

Sample code	BET specific surface area ($m^2 \, g^{-1}$)	Total pore volume ($cm^3 \, g^{-1}$)	Micropore area (t-plot) ($m^2 \, g^{-1}$)	Micropore volume (t-plot) ($cm^3 \, g^{-1}$)	Mesopore volume ($cm^3 \, g^{-1}$)	V_{meso}/V_{total} [%]	Average pore size (nm)
HPAC	1393	0.73	1335	0.66	0.07	9.6	2.1
EPAC	1537	0.98	1392	0.81	0.17	17.4	2.6

This is because of the harsher hydrothermal treatment, which results in swelling and loosening of the cellulose microfibrils [33]. Further, the absence of any sharp XRD peaks and the presence of two broad peaks indicate the highly disordered nature i.e. lower percentage of crystalline graphitic domains in both the carbon powders, however, the HPAC is more disordered (amorphous) as compared to EPAC powder.

The Raman spectra of both types of activated carbons (EPAC and HPAC) are shown in Fig. 4(D). Two prominent peaks, corresponding to D and G bands, are observed typically at $1340 \, cm^{-1}$ and $1594 \, cm^{-1}$, respectively, for both the carbon samples. A broad and relatively weak peak between 2300 and $3100 \, cm^{-1}$ has also been observed for both the carbons. The G-band is attributed to the tangential vibrations of sp^2 bonded graphitic structure [45], whereas the D-band is associated with the presence of disorder, defects and 6-fold aromatic rings in the carbon materials [46]. The intensity ratio of D and G peaks (i.e., I_D/I_G ratio) has also been estimated (after de-convolution of Raman bands) and found to be ~ 1.44 and ~ 0.95 for EPAC and HPAC materials, respectively. The values of I_D/I_G have been correlated with the crystallite size of both the carbons, and found that EPAC has nanocrystalline carbon containing more graphitic sheets, whereas HPAC has predominantly

amorphous carbon due to disruption in the ordered aromatic ring clusters and haphazardly distributed graphitic sheets [47]. The Raman broad peak can be seen to consist of two peaks centered at $2670 \, cm^{-1}$ and $2890 \, cm^{-1}$, attributed to 2D and D + G bands [48] respectively (Fig. 4(D)). These are also indicative of the presence of disorder/defects in the carbon materials.

3.3. Performance studies of EDLCs

The electrochemical performance of quasi-solid state EDLCs have been studied by EIS, CV and GCD techniques. The EDLCs were fabricated using flexible gel polymer electrolytes GPE-1 and GPE-2 films, and EPAC and HPAC electrodes, as mentioned in the experimental section.

3.3.1. EIS studies

The EIS (Nyquist) plots for the EDLC cells (Cell #1 to Cell#4) for the frequency range from 10 mHz to 100 kHz are shown in Fig. 5. The steeply rising nature of the EIS (i.e. Z″ versus Z′) plots in the middle-to lower frequency region (almost parallel to Z″-axis) indicate the
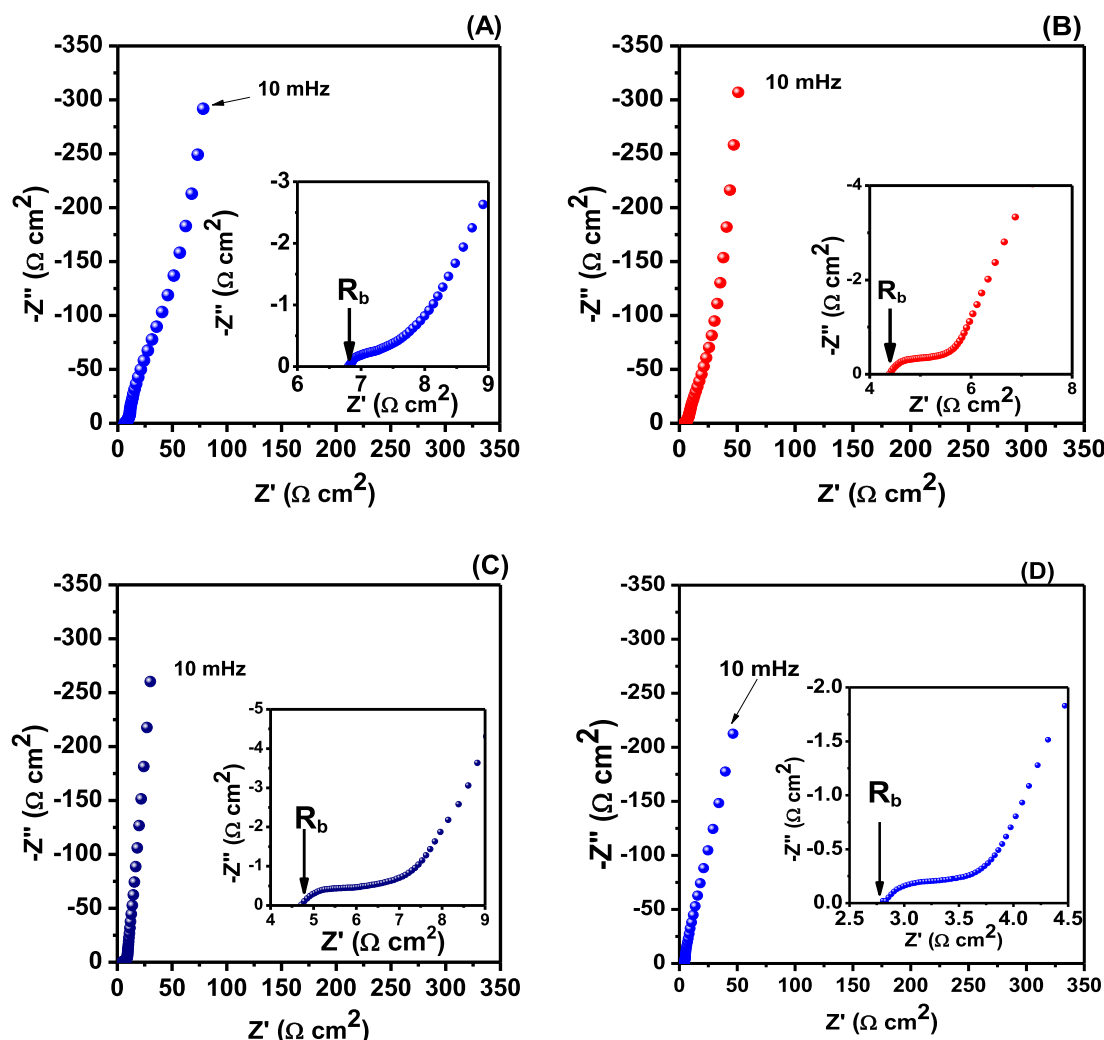
Fig. 5. EIS plot of EDLC cells: (A) Cell#1, (B) Cell#2, (C) Cell#3, and (D) Cell#4, recorded at room temperature in the frequency range 100 kHz to 10 mHz. Expanded EIS plots in high-frequency region are shown in insets.

capacitive behaviour of all the EDLC cells. The expanded representations of EIS plots in the high to middle frequency range are shown as insets of Fig. 5. A subdued curved region is present in the high frequency region of the EIS plot of each cell, which is associated with resistive/transmission line behavior [49–51]. The bulk resistance of cells (R_b), which includes the resistances of electrodes and electrolyte, is estimated from Z′-axis intercepts in the high frequency region, as shown by arrows in Fig. 5(insets). In the middle frequency region, the effect of Warburg impedance, caused by the finite diffusion limit of electrolyte ion transport in the porous carbon electrodes is also observed.

The specific capacitance (C_{sp}) of each EDLC cell was evaluated by using the equation $C_{sp} = 2/(\omega \times m \times |Z''|)$, where Z'' is the imaginary part of the impedance (Z) of the cell, ω is the angular frequency and m is the mass of single electrode (excluding the masses of binder and conductive additive acetylene black) [50,51]. The values of C_{sp}, the resistive parameters R_b and R (resistance at 10 mHz) and knee frequency are listed in Table 3. The knee frequency is defined as the frequency below which the device is considered to be fully in the capacitive domain.

A comparison indicates that the resistive parameters, particularly cell resistance R_b, are lower for Cell#2 and Cell#4 (with EPAC electrodes) relative to those for Cell#1 and Cell#3 (with HPAC-electrodes).

Table 3
Various electrical parameters of EDLC cells from EIS studies.

EDLC cells	R_b (Ω-cm^2)	R (Ω-cm^2)	C_{sp} (F g^{-1})	Knee freq. (Hz)
Cell-1	7.7 ± 0.7	46 ± 3	113 ± 1	1.77 ± 0.01
Cell-2	4.4 ± 0.2	48 ± 1	118 ± 2	1.40 ± 0.12
Cell-3	3.9 ± 0.6	36 ± 6	148 ± 8	1.21 ± 0.18
Cell-4	2.6 ± 0.2	29 ± 5	168 ± 5	1.50 ± 0.21

This indicates the facile switching of electrolyte ions in EPAC-electrodes as they have higher content of mesoporosity and larger average pore size as compared to HPAC-electrodes (Table 2). The significant influence of nature of electrodes and electrolytes on the specific capacitance values can be seen distinctly. The Cell#2 (with EPAC electrodes and GPE containing only IL) offers slightly higher specific capacitance (Table 3) with respect to Cell#1 (with HPAC electrodes and same electrolytes). This is possible due to slightly higher specific surface area of EPAC as compared to HPAC (Table 2). On the other hand, the Cell#3 and Cell#4 with GPE-2 films (incorporated with Mg-salt) offer substantial enhancement (1.3–1.4 times) in C_{sp} (Table 3). This indicates that Mg^{2+} ions, which are smaller in size ($r_{Mg^{2+}} \sim 0.72$ Å), form capacitive double layers even with smaller porous interiors of activated carbon, which are not accessible to bigger size electrolyte ions (anions

Table 4
EDLCs using different biomass-based electrodes.

S. no.	Biomass material	Activating agent	BET Surface area (m^2g^{-1})	Electrolyte used	Specific capacitance (F/g^{-1})	Ref.
1.	Peanut shell	NaOH,	552	KOH	233	52
		Physical activation	726	KOH	378	
2.	Coconut shell	$ZnCl_2$	2100	BMPTFSI/SN/PVdF-HFP	210–240	13
				EMITf/SN/PVdF-HFP	230–254	
3.	Waste paper	HNO_3	463	KOH	232	53
4.	Almond shell	$CaCl_2$	214	PVdF-HFP/PC/$MgClO_4$/(EDiMIM) [BF_4]	203	54
5.	Waste coffee ground	$ZnCl_2$	940–1021	$MeEt_3NBF_4$/AN	100	55,56
			1091	H_2SO_4	368	
6.	Celtuce leaves	KOH	3400	2 M KOH	421	40
					273	
7.	Coffee shells	$ZnCl_2$	842	KOH	150	14
8.	Rice husk	NaOH	1886	KCl	210	57
		KOH	1392		180	
9.	Walnut shells	Physical/chemical activation	1197	KOH	292	58
10.	Sunflower seed shells	KOH	1371–2821	KOH	311	59
11.	Pistachio shells	Steam	1009	HNO_3 & H_2SO_4	60–125	60,61
		KOH + CO_2	1013–2145	H_2SO_4 & $NaNO_3$	25–47	
13.	Cherry stone waste	KOH	1100–1300	H_2So_4, $MeEt_3NBF_4$/CH_3CN	230	62
14.	Banana fiber	$ZnCl_2$, KOH	686,1097	Na_2So_4	74,66	63
15.	Potato starch	KOH	2342	KOH	335	64
16.	Peanut shell	$ZnCl_2$	1527–1634	1 M Et_4NBF_4 in PC	74–99	65
17.	Peanut shell	KOH	956–3616	H_2SO_4	356	66
18.	Peanut shell	KOH	2070	H_2SO_4	186	67
19.	Peanut shell	$ZnCl_2$	1411	PVdF-HFP/EMITf	148	**Present work**
			1483	PVdF-HFP/EMITf/Mg $(Tf)_2$	168	

of salt and/or component ions of IL). With Mg-salt based GPE film also, EPAC electrodes show superior behavior, offering higher capacitance value as compared to that with HPAC-electrodes. Thus the EPAC electrodes interfaced with Mg-salt incorporated GPE film (Cell#4) shows optimum capacitance of $168 \, F \, g^{-1}$, which is comparable or higher than many solid-state/quasi-solid-state EDLCs [13,14,40,52–67]. However, liquid electrolyte based capacitors show mostly higher capacitance. Table 4 shows a comparison of specific capacitance values of the present peanut-shells based EDLCs with their activated carbon prepared from different biomasses including the peanut shells reported by other worker.

The rate capability of the supercapacitors is an important aspect to consider, which is directly associated with the specific power and cyclic performance. The rate performance of EDLCs has been evaluated in terms of knee frequency (as defined above), response time (τ_o) and pulse-power (also referred as "figure of merit") of supercapacitors [68]. The specific pulse power of cells has been estimated by $P_o = E_o/\tau_o$, where E_o is specific energy density at f_o (response frequency), and τ_o is the response time which is reciprocal of response frequency at phase angle ~45° at which the imaginary and real part of impedance are equal [69]. Fig. 6(A) depicts a typical plot of Z'and Z″ against frequency (Bode plot) for an EDLC cell (Cell#4). The related parameters namely f_o, τ_o, E_o and P_o have been estimated for each cell and listed in Table 5. The response time (τ_o), which basically represents the average switching time of insertion-deinsertion through the porous carbon electrodes, is found to be smallest (~0.9 s) and hence leads to highest specific pulse power (~$41.6 \, Wh \, kg^{-1}$) for Cell#4. This indicates the superiority of the EPAC, having higher mesoporous interiors, over the HPAC electrodes from the rate capability point of view and also due to relatively facile insertion-deinsertion of electrolyte ions (including Mg^{2+} ions) through micro-/mesopores of EPAC electrodes.

Fig. 6(B) shows the phase angle variation with frequency for all the cells (Cell#1 to Cell#4). It may be noted that an ideal capacitor cell shows the phase angle of 90° for entire frequency range, shown by a horizontal line in Fig. 6(B). EDLC cells#1–4, in the present case, show phase angle 86.9°, 82.0°, 83.4° and 77.7°, respectively, in the lower frequency regime. This is indicative of the capacitive behaviour of the

cells for lower frequency range only, as indicated from Nyquist plots also (Fig. 5), discussed above.

To further evaluate the ion diffusion kinetics and rate performance, the real and imaginary capacitances (C′ and C″) have been plotted as a function of frequency for all the cells, as depicted in Fig. 6(C and D). The values of C′ and C″ have been evaluated from the frequency dependent Z′ and Z″ values according to the following expressions [70]:

$$C'(\omega) = \frac{-Z''(\omega)}{\omega|Z(\omega)|^2} \tag{2}$$

$$C''(\omega) = \frac{Z'(\omega)}{\omega|Z(\omega)|^2} \tag{3}$$

The slope of the variation of C' versus frequency is almost zero in high-frequency region from 10-10^5 Hz. Below 10 Hz, a fast increase in C' values is observed up to 0.1 Hz, thereafter, these values tend towards saturation. This is expected, as C' is the real capacitance of the cell, and its value tends to the constant current capacitance value at very low frequencies [71].

On the other hand, C″ versus frequency plots show two-peak feature in the frequency range from 10^{-2} to 10^2 Hz. It may be noted that the AC-based EDLCs show single peak, in general, as reported in literature [72–74]. The C″ plot is related to relaxation processes due to irreversible processes, which cause losses in supercapacitors [70]. The peak at frequency (f_o) in the C″ Bode plot indicates transition between resistive (above f_o) and capacitive (below f_o) nature of the capacitor. The influence of various factors i.e. difference between the amount of meso- and micropores, their average sizes and the type of electrolytes on the C″ Bode plots for all the cells is explained as follows.

Out of the two peaks, the peak at lower frequency can be assigned to slower relaxation processes occurring in micropores, while the peak at higher frequency to faster processes in the mesopores, where ions have ample space for movement. This is the reason, both the C″-peaks are observed at relatively higher frequencies in the EPAC-electrodes (having higher amount of mesopores) as compared to that of HPAC-electrodes (Fig. 6(D)). It has been further observed that the bimodal peaks for both the electrodes shift towards lower frequencies when the
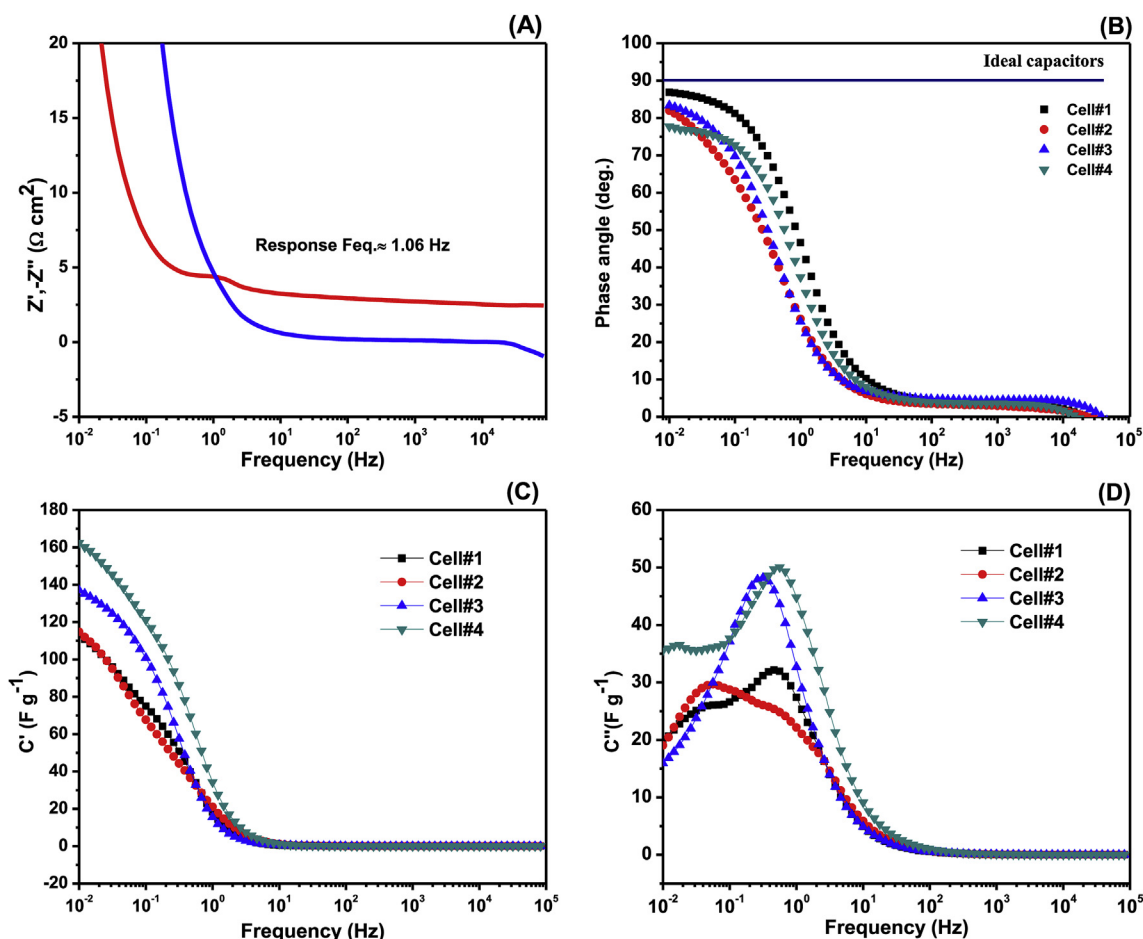
Fig. 6. (A) Real and imaginary impedances versus frequency plots (Bode plots) for a typical cell (Cell#4), (B) phase angle, (C) real capacitance (C′), and (D) imaginary capacitance (C″) versus frequency for all the cells.

Table 5
Rate performance parameters from EIS studies.

EDLC cells	Response frequency f (Hz)	Response time (sec)	Available Specific Energy (Wh kg^{-1})	Pulse power (kW kg^{-1})
Cell-1	0.60	1.6	6.7	14.49
Cell-2	0.90	1.1	12.05	39.06
Cell-3	0.74	1.3	8.95	23.86
Cell-4	1.06	0.9	10.90	41.58

GPE-2 (containing Mg-salt) is employed, as compared to the EDLCs incorporated with GPE-1 (without Mg-salt). This is owing to the increased viscosity of GPE-2 due to Mg-salt addition.

3.3.2. CV studies

The electrochemical performance of the quasi-solid-state EDLCs has also been tested by cyclic voltammetry (CV). The comparative CV patterns for all the four cells have been recorded at 10 mV s^{-1} at room temperature and depicted in Fig. 7(A). A comparison of Cell#1 and Cell#2, fabricated respectively with HPAC and EPAC electrodes, and the electrolyte GPE-1 (without Mg-salt) indicates the superior capacitive performance of Cell#2 showing better rectangular shape (i.e. less resistive) as compared to Cell#1. This indicates the superior capacitive performance of EPAC-electrodes over the HPAC–electrodes. The Cell#3 and Cell#4, which employ GPE-2 (with Mg-salt) as electrolyte, show similar behaviour. However, higher voltammetric currents, hence, higher specific capacitance values have been obtained for these cells. A further comparison indicates that the CV pattern for Cell#4 turns out to be the best amongst the four cells, offering highest voltammetric

current and hence optimum specific capacitance. This is in conformity with the EIS results, as discussed above. The enhanced specific capacitance in Cell#4 is attributed to the fast insertion/de-insertion of small Mg^{2+} ions through even the smaller pores of the EPAC-electrodes along with the other electrolyte ions through their larger pores.

Fig. 7(B) shows the CV patterns of a typical cell (Cell#4) with a gradual increase in the voltage range from 1.0 to 2.0 V, recorded for the scan rate of 5 mV s^{-1}. It may be noted that the shape of the CV curves remains almost rectangular with increasing voltage limit, applied to the Cell-4. This observation shows the wider electrochemical potential range (from 0 to 2.0 V) of the gel electrolyte containing Mg-salt. This working voltage range has further been confirmed in charge-discharge studied, discussed below.

The scan rate dependent CV patterns have been recorded for all the cells (Cell#1 to Cell#4) up to the scan rate of 1000 mV s^{-1}, as typically shown in Fig. 7(C) for Cell#4 (with EPAC-electrodes and Mg-salt containing GPE-2). The scan rate dependent CV patterns for the other cells are shown in Fig. S1-S3. The rectangular shape of the voltammograms has been observed for Cell#4 up to the higher scan rate of 1000 mV s^{-1} (Fig. 7(C)). This indicates the fast switching behaviour of electrolyte ions through porous electrodes i.e. high rate capability of the cell. Cell#2 (interfaced with EPAC-electrodes and GPE without Mg-salt) also shows almost similar CV responses as Cell#4. On the other hand, Cell#1 and Cell#3 (with HPAC-electrodes) show relatively tilted CV responses (Fig. S1-S3) at scan rate of 1000 mV s^{-1}. This confirms that the porous texture of EPAC electrodes (with suitable ratio of meso- and microporosity) shows better rate performance as compared to HPAC-electrodes, which possess predominantly microporous interiors. The highest rate performance of the Cell#4 has also been indicated in EIS
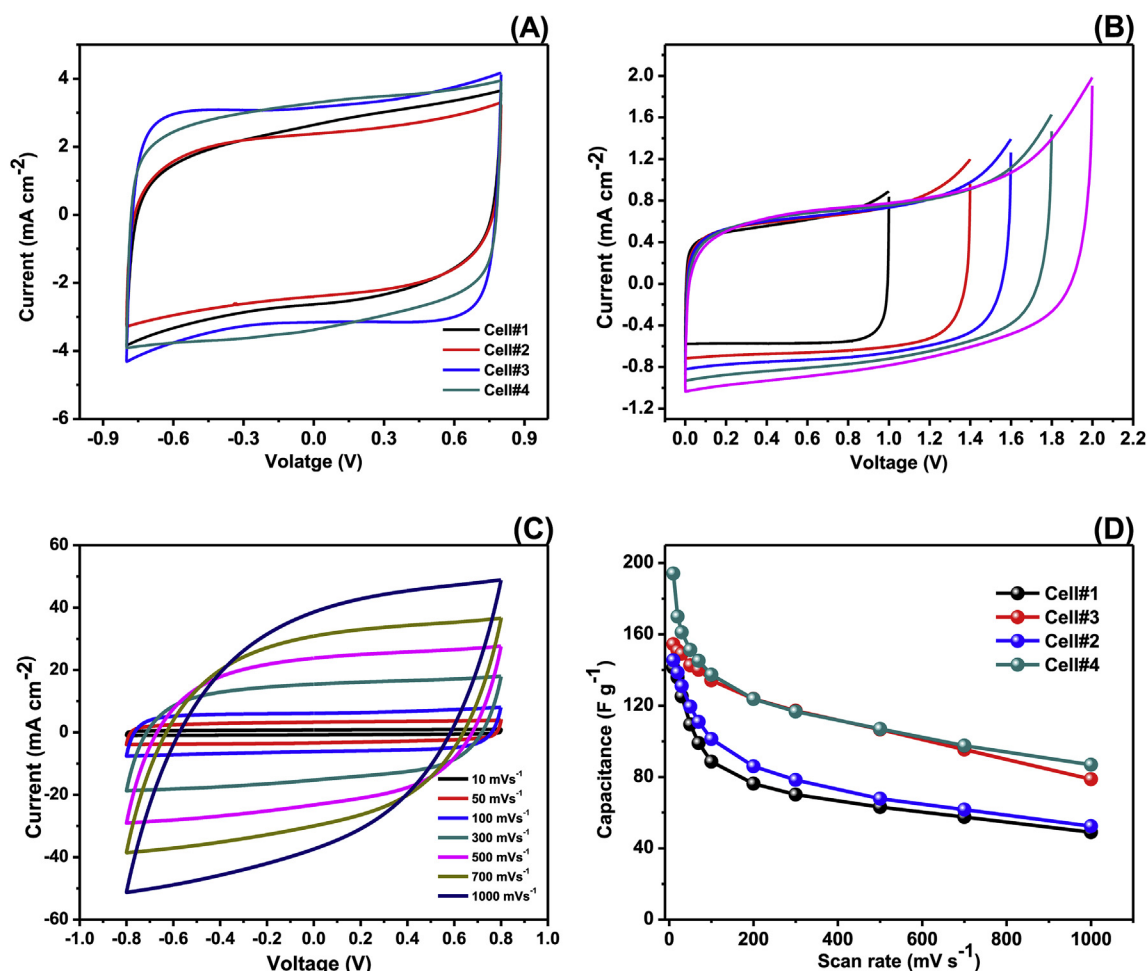
Fig. 7. (A) Comparative CV responses of all the EDLC cells at a scan rate $10 \, \text{mV s}^{-1}$, (B) CV pattern of Cell#4 with gradual increase in voltage range recorded at a scan rate $10 \, \text{mV s}^{-1}$, (C) CV patterns recorded at different scan rates for Cell#4, and (D) variation of specific capacitance (C_{sp}) as a function of scan rates for all the cells.

studies; discussed earlier in terms of response time, pulse power, etc. The highest rate performance of Cell#4 is attributed to the synergic effect of the suitable porous texture of EPAC-electrodes and small size of the Mg^{+2} ions. A slight tilt in voltammogram, observed beyond the scan rate of $700 \, \text{mV s}^{-1}$, is due to a finite value of equivalent series resistance (ESR) of the cell.

Fig. 7(D) shows the scan rate dependence of specific capacitance C_{sp}, evaluated from CV responses using the expression: $C_{sp} = i/s$, where i is the voltammetric current at the middle of the response and s is the scan rate. Each cell shows initial fast decrease followed by a gradual decrement in C_{sp} beyond the scan rate of $100 \, \text{mV s}^{-1}$. The Cell#3 and Cell#4 show significantly higher specific capacitance even beyond $100 \, \text{mV s}^{-1}$ and up to $1000 \, \text{mV s}^{-1}$. This indicates the effect of Mg-salt incorporation in GPE employed in capacitor cells.

3.3.3. Galvanostatic charge-discharge

Galvanostatic charge-discharge (GCD) measurements have been performed on all the cells (Cell#1 to Cell#4). Fig. 8(A) shows GCD profiles for all the cells (Cell#1 to Cell#4), recorded at a current density of $1.0 \, \text{mA cm}^{-2}$ ($\sim 1.25 \, \text{A g}^{-1}$). All these cells show almost triangular shaped GCD profiles, indicating the charge storage due to proper electrical double layer formation at the interfaces [3]. In order to optimize the voltage range of charging, the charge-discharge tests have been carried out on a typical cell (Cell#4) for varying voltage steps between 0 and 2.5 V at a constant current of $1.0 \, \text{mA cm}^{-2}$ ($\sim 1.25 \, \text{A g}^{-1}$), as shown in Fig. 8(B). The optimum voltage range for

efficient charge-discharge has been found to be 0–2.0 V, beyond that, the triangular shape is deviated and the columbic efficiency reduces substantially from 81% to 65%. In further GCD studies, all the cells have been charged up to a maximum voltage of 2.0 V.

The values of ESR (internal resistance) of the cells have been estimated by voltage drop (ΔV), observed in discharge curves, using the expression: $\text{ESR} = \Delta V/2i$, where i is a constant current [73]. The discharge capacitance (C_d) of each cell has been evaluated from the linear portion of the discharge curves using the expression: $C_d = (i \times \Delta t)/\Delta V$, where Δt is the discharge time interval for a voltage range of ΔV. The specific capacitance (C_{sp}) of the single electrode has been determined by: $C_{sp} = 2C_d/m$, where 'm' is the mass of the activated carbon employed in single electrode, excluding the mass of current collector, binder and conductive additive (AB). The values of ESR and C_{sp} are listed in Table 6.

The ESR values of Cell-1 and Cell-2 with GPE-1 (without Mg-salt) are found to be about 1.5–2.0 times higher as compared to Cell-3 and Cell-4 with Mg-salt incorporated GPE-2 films. This confirms the effect of facile switching behavior of smaller Mg^{2+} ions at the interfaces forming double layers with both types of EDLC-electrodes (HPAC and EPAC). The specific capacitance (C_{sp}) of Cell-3 and Cell-4 (with Mg-salt incorporated GPE-2 films) has also been found to be ~ 1.5 times higher as compared to that of Cell-1 and Cell-2 with GPE-1 (without Mg-salt) (Table 6). This further confirms the improved formation of double layer with Mg-salt incorporated electrolyte GPE-2. It has been noticed that the activated porous carbon prepared through the process of ethanol
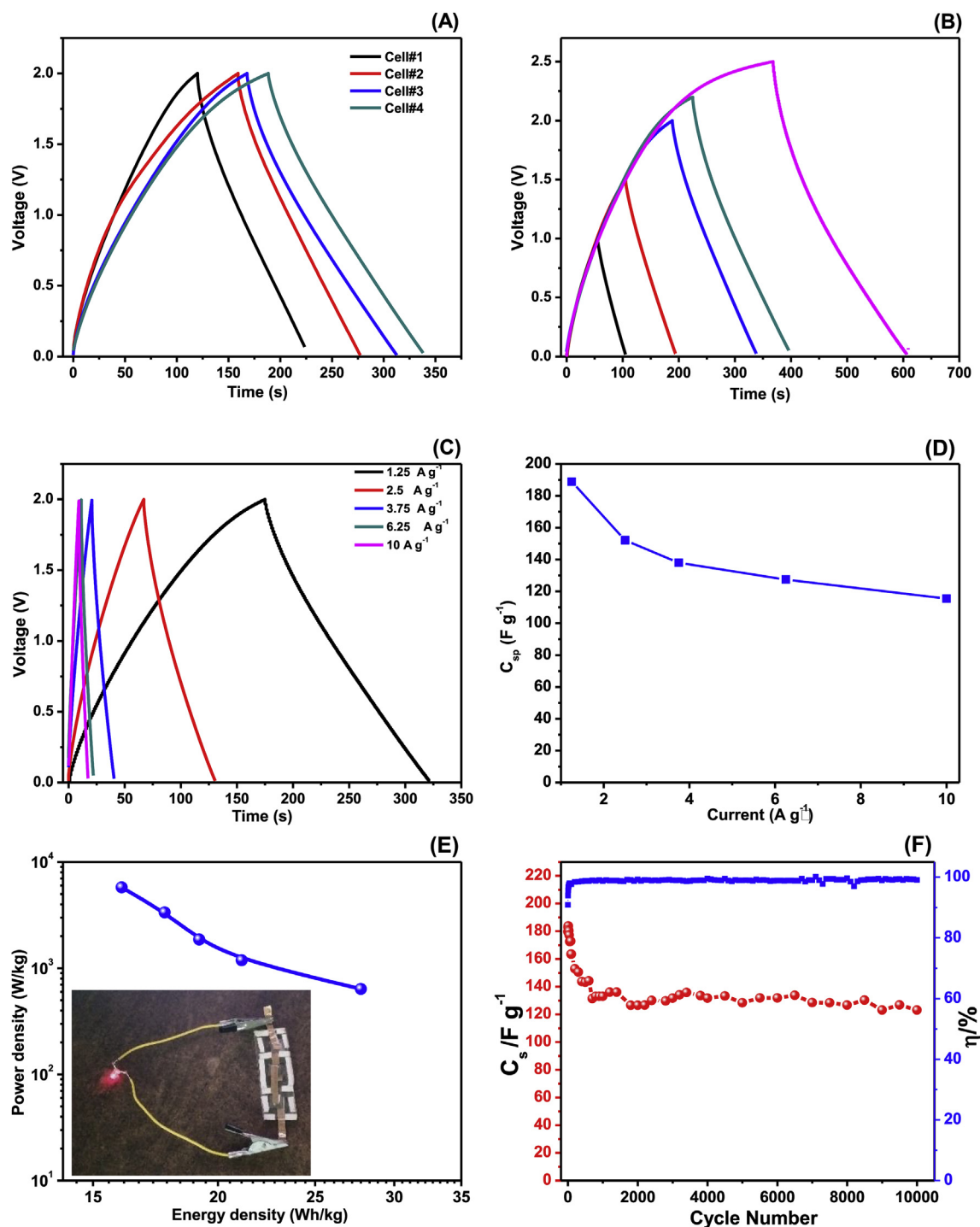
Fig. 8. (A) Comparative charge-discharge curves for all the EDLC cells at current density of 1.25 A g^{-1}, (B) galvanostatic charge-discharge profiles of a typical cell (Cell#4) for different voltage ranges, recorded at a current density of 1.25 A g^{-1}, (C) charge-discharge profiles of a typical cell (Cell#4) at different current densities, (D) specific capacitance of Cell#4 as a function of current density, (E) Ragone plot for a typical cell (Cell#4) (inset shows lighting of an LED by three cells in series), (F) Specific capacitance and Coulombic efficiency versus charge-discharge cycles, recorded at constant current 1.25 Ag^{-1}.

soaking i.e. EPAC-electrodes show higher specific capacitance as compared to hydrothermally prepared HPAC-electrodes with both the GPEs, with and without Mg-salts (Table 6). This is owing to supportive combination of micro- and mesoporous interiors in EPAC-electrodes, which provide suitable pathways for facile movement of electrolyte ions (including Mg^{2+} ions along with component ions of IL).

Fig. 8(C) depicts the GCD profiles of a typical cell (Cell#4) at different current densities in the voltage range of 0–2 V. The specific capacitance (C_{sp}) has been evaluated as a function of current densities, as

shown in Fig. 8(D), which directly indicates the rate performance of the device. It may be noted that after a fast initial fading of ∼ 27% up to the current density of 2.5 A g^{-1}, a gradual decrease in C_{sp} has been observed up to the current density 10 A g^{-1}. The fast fading at lower current is observed possibly due to the slow kinetics of the electrolyte ions at the interfaces [75]. The gradual decrease in specific capacitance for larger current densities indicates the faster discharge rates of the device. The larger pores (mesopores), present in EPAC-electrodes, accelerate the electrolyte ion transfer, as a result a less fading in C_{sp} is

Table 6
Charge-discharge characteristics of EDLC cells at a constant current density of $1.0\,\mathrm{mA\,cm^{-2}}$ ($125\,\mathrm{A\,g^{-1}}$).

EDLCcells	ESR (Ω-cm^2)	Specific capacitance C_{sp}(F g^{-1})	Specific energy (Wh kg^{-1})	Max. Power density (kW kg^{-1})
Cell-1	15	109	14.9	32
Cell-2	20	127	17.9	32
Cell-3	10	168	23.4	56
Cell-4	10	189	26.0	57

observed and a better rate performance is achieved.

The specific energy (E), maximum power density (P_{max}), and effective power density (P_{eff}) of the EDLCs have also been estimated from their charge-discharge profiles using the following expressions:

$$E = \frac{1}{2M}C_d V^2 \qquad (4)$$

$$P_{max} = \frac{V^2}{4M \times ESR} \qquad (5)$$

$$P_{eff} = \frac{E}{t} \qquad (6)$$

where, V is optimum voltage and M is the mass of the activated carbon used in both the electrodes of the cells and t is time (in sec). The values of E and P_{max} of all the cells (Cell#1- Cell#4), evaluated at current density $1.0\,\mathrm{mA\,cm^{-2}}$ ($1.25\,\mathrm{A\,g^{-1}}$), are listed in Table 6. The optimum value of E and P_{max} has been observed for Cell#4 (Table 6). This further indicates the synergic effect of hierarchical porous carbon in EPAC-electrodes and Mg^{2+} ion conducting gel polymer electrolyte (GPE-2). The value of E and P_{max} for the optimized cell (Cell-4) is reported to be 26 Wh kg^{-1} and 57 kW kg^{-1}, respectively, which is substantially higher than many gel polymer electrolyte based flexible EDLCs fabricated employing AC electrodes. For example, Yang et al. [76] reported an all solid-state EDLC based on composite carbon electrodes and alkaline polymer electrolyte (PVA/KOH) offering specific energy of 10 Wh kg^{-1} at 29.6 kW kg^{-1}. Pandey et al. [73] recently reported a solid-state EDLC with commercial AC powder electrodes and GPE film based on succinonitrile and IL, which possesses high specific energy of 36 Wh kg^{-1} with maximum power of 24.5 kW kg^{-1}. A polymer/IL blend electrolyte PVdF-HFP/[PMpyr] [NTf$_2$] has recently been reported to fabricate an EDLC with AC-electrodes, which offers high specific energy ($\sim$30.7 Wh kg^{-1}) but at lower power density (4.13 kW kg^{-1}) [77]. Another recent report on solid-state EDLC, based on IL incorporated PEO cross-linked GPE, coupled with AC-electrodes, shows moderate specific energy ($\sim$16 Wh kg^{-1}) with low value of power density ($\sim$1.1 kW kg^{-1}) [78]. Our group recently reported AC-based EDLC with flexible porous polymer electrolyte (PVdF-HFP/EC/PC/NaClO$_4$), which offers E and P values of 17.7 Wh kg^{-1} and 14.3 kW kg^{-1}, respectively [79]. Another solid-state EDLC cell, reported by us, fabricated with activated charcoal electrodes and IL incorporated PVdF-HFP/LiTf/EMITf/EC-PC GPE film, offers E and P values of 6.81 Wh kg^{-1} and 4.91 kW kg^{-1}, respectively [29].

Fig. 8(E) shows the Ragone plot i.e. specific energy (E) versus effective power (P_{eff}) of a typical EDLC cell (Cell#4), which shows the expected profile similar to the EDLCs/supercapacitors, reported in literature [80,81]. For specific energy variation from $\sim$16 to $\sim$28 Wh kg^{-1}, the effective power density has been reduced by 10-fold only from $\sim$5.7 to 0.6 kW kg^{-1}, which is an excellent profile of an EDLC. The inset of Fig. 8(E) shows the glow of LED by the charged capacitor cells (Cell-4). Three capacitors cells, connected in series, were used to light the LED. The 38–50 mW LED of 5 mm size glowed for $\sim$80 s before its fading. This indicates the enough energy storage ability of the cells.

Due to its optimum performance, Cell#4 has been selected for prolonged cyclic test. Fig. 8(F) shows the variation of discharge specific capacitance (C_{sp}) and Coulombic efficiency (η%) as a function of charge-discharge cycles. Coulombic efficiency (η%) of the EDLC was evaluated by: $\eta = t_D/t_C \times 100\%$, where t_D and t_C are the duration of discharging and charging, respectively [82]. The cycling performance has been evaluated for charge-discharge of the cell between 0 and 1.0 V at a current density of 1.25 A g^{-1}. It may be noted that after initial $\sim$28% fading for about 1000 cycles, almost stable specific capacitance has been observed up to 10000 cycles. The initial decline is possibly due to the formation of a passivation layer at the electrode-electrolyte interfaces. The cell stabilizes and capacitance-fading stops as various electrochemical processes equilibrate with each other. This is further confirmed from the observed value of Coulombic efficiency of the cell, which is $\sim$98% for 10000 charge-discharge cycles.

3.4. Temperature dependent performance

The performance of EDLC cell has been tested as a function of temperature. The EIS and CV measurements have been performed on an optimized cell (Cell#4) in the temperature range from -50 to 70 °C in the dynamic nitrogen atmosphere. The EIS/CV responses and values of C_{sp} (evaluated from these responses) as a function of temperature are shown in Fig. S4(a-c). The EIS plots maintain the shape, which is usually observed for EDLCs/supercapacitors, for all the temperatures (Fig. S4-a). This indicates that the fundamental charge-storage mechanism and capacitive nature in the EDLC is not altered in the temperature range from -50 to 70 °C. The CV curves (recorded at the scan rate of 20 mV s^{-1}) are almost rectangular for all the temperatures under the present study (Fig. S4-b). This further indicates that the capacitive nature of the device is maintained in both the low temperature and high temperature zones. This appears to be due to the suitable pore shape and size-distribution in EPAC-electrodes, which allows fast ion transport to the surface, and efficient ion-transfer at the interface. The CV curves tends to be better rectangular shaped as the temperature increases, most possibly due to decrease in the viscosity of the liquid electrolyte entrapped in GPE, which improves the ion-diffusion dynamics. Variations of C_{sp}, evaluated from both EIS and CV, are observed to be similar, and show a gradual increase with temperature indicating thermal stability of the device from -50 to 70 °C (Fig.S4-c). The temperature dependent performance of the optimized EDLC (Cell#4) has been found to be comparable or even superior to many reports on similar systems. For example, Łatoszyńska et al. [83] reported the continuous increase in specific capacitance of porous carbon electrode based capacitor with proton conducting based gel polymer electrolyte (evaluated from CV) from $\sim$48 F g^{-1} to $\sim$88 F g^{-1} for temperature change from -40 °C to 80 °C due to increase in electrolyte conductivity. Similarly, Negre et al. [84] reported a solid-state supercapacitor with activated carbon electrodes and a mixed ionic-liquid in SiO$_2$ matrix based ionogel and showed the increase in capacitance with temperature from $\sim$8 F g^{-1} at -40 °C to $\sim$90 F g^{-1} at 60 °C. Pandey et al. [31], from our laboratory, reported temperature dependent performance of an EDLC fabricated from MWCNT electrodes and GPE PVdF-HFP/ionic liquid/Mg-salt and found the variation in specific capacitance (evaluated from EIS) from $\sim$31 F g^{-1} at 0 °C to $\sim$46 F g^{-1} at 60 °C. The value of capacitance dropped to $\sim$37 F g^{-1} at 70 °C but did not decrease much beyond this temperature. In another studies, Pandey et al. [73] reported a variation of specific capacitance from 91 F g^{-1} at -30 °C to 116 F g^{-1} at 80 °C for solid state EDLC, fabricated with GPE comprising succinonitrile/ionic liquid/PVdF-HFP and activated carbon electrodes. Recently, another study of our group showed a similar trend in specific capacitance variation from 90 F g^{-1} to 118 F g^{-1}, when temperature was varied between 0 °C and 80 °C for EDLC cells, prepared with porous polymer electrolyte and activated carbon electrodes [79].

4. Conclusions

Porous activated carbons (ACs) have been derived from peanut-shells following two different pretreatments and employed as electrodes to fabricate symmetric quasi-solid-state EDLCs. Morphological, spectroscopic and surface area/porosity analyses have been performed to characterize porous AC-electrodes. The Mg-salt (Mg (Tf)$_2$) and IL (EMITf) incorporated GPE-films were used as electrolytes/separators of the devices. Performance of EDLCs have been characterized using EIS, CV, and galvanostatic charge-discharge tests. The following conclusions can be drawn from the above studies:

(1) The ethanol soaked peanut-shells-based AC (EPAC) possesses predominantly higher mesoporous interiors as compared to hydrothermally prepared AC (HPAC). Pre-soaking of peanut-shells in ethanol converts micropores to wide range of mesopores and substantially enhanced the total pore volume.

(2) As indicated from Raman studies, EPAC has nanocrystalline carbon containing more graphitic sheets, whereas HPAC is predominantly amorphous carbon.

(3) The free-standing, flexible film of GPE Mg (Tf)$_2$/EMITf/PVdF-HFP, offering excellent ESW of ~ 3.7 V (-1.0–2.7 V) and room temperature ionic conductivity of $\sim 3.8 \times 10^{-3}$ S cm^{-1}, shows its suitability as electrolyte/separator in EDLCs. The effect of Mg^{2+}-ions on the performance of supercapacitors has been investigated.

(4) The EPAC electrodes offer better capacitive performance over the HPAC electrodes. Mg-salt incorporated GPE film provides substantially (1.3–1.4 times) enhanced specific capacitance as compared to that with only IL containing GPE, indicating the role of Mg^{2+} ions forming double layers with even smaller pores.

(5) Higher mesoporous nature of EPAC-electrodes and facile insertion-extraction of electrolyte ions through porous electrodes provide high rate performance of the device.

(6) The EDLC cell with EPAC electrodes and Mg-salt/IL incorporated GPE film shows optimum performance in terms of specific capacitance (~ 189 F g^{-1}), specific energy (~ 26 Wh kg^{-1}) and maximum specific power (~ 57 kW kg^{-1}).

(7) Cycling test up to $\sim 10,000$ charge-discharge cycles shows the stable performance of the EDLC cell with $\sim 100\%$ Coulombic efficiency and $\sim 28\%$ initial fading in specific capacitance.

(8) The EDLC shows thermally stable performance in the temperature range from -50 to $70\,°C$.

(9) Studies indicate the excellent supercapacitive nature of the novel interface of EPAC electrodes and Mg-salt/IL incorporated flexible GPE films.

Acknowledgements

Appendix A. Supplementary data

Supplementary data to this article can be found online at https://doi.org/10.1016/j.jpowsour.2018.09.032.

References

[1] V. Etacheri, R. Marom, R. Elazari, G. Salitra, D. Aurbach, Challenges in the development of advanced Li-ion batteries: a review, Energy Environ. Sci. 4 (2011) 3243–3262.

[2] B.K. Kim, S. Sy, A. Yu, J. Zhang, Electrochemical supercapacitors for energy storage and conversion, Handbook of Clean Energy Systems, vol. 5, John Wiley & Sons, 2015.

[3] B.E. Conway, Electrochemical Supercapacitors: Scientific Fundamentals and Technological Applications, Kluwer Academic/Plenum Publisher, New York, 1999.

[4] S. Iijima, Helical microtubules of graphitic carbon, Nature 354 (1991) 56–58.

[5] D.S. Bethune, C.H. Kiang, M.S. De Vries, G. Gorman, R. Savoy, J. Vazquez, R. Beyers, Cobalt-catalysed growth of carbon nanotubes with single-atomic-layer walls, Nature 363 (1993) 605–607.

[6] D. Hongjie, A.G. Rinzler, P. Nikolaev, A. Thess, D.T. Colbert, R.E. Smalley, Single-wall nanotubes produced by metal-catalyzed disproportionation of carbon monoxide, Chem. Phys. Lett. 260 (1996) 471–475.

[7] C.T.J. Low, F.C. Walsh, M.H. Chakrabarti, M.A. Hashim, M.A. Hussain, Electrochemical approaches to the production of graphene flakes and their potential applications, Carbon 54 (2013) 1–21.

[8] W. Lochananon, D. Chatsiriwech, Effect of phosphoric acid concentration on properties of peanut shell adsorbents, J. Ind. Eng. Chem. 14 (2008) 84–88.

[9] C. Tran, V. Kalra, Fabrication of porous carbon nanofibers with adjustable pore sizes as electrodes for supercapacitors, J. Power Sources 235 (2013) 289–296.

[10] X. He, N. Zhao, J. Qiu, N. Xiao, M. Yu, C. Yu, X. Zhang, M. Zheng, Synthesis of hierarchical porous carbons for supercapacitors from coal tar pitch with nano-Fe$_2$O$_3$ as template and activation agent coupled with KOH activation, J. Mater. Chem. 1 (2013) 9440–9448.

[11] V. Presser, M. Heon, Y. Gogotsi, Carbide-derived carbons–from porous networks to nanotubes and graphene, Adv. Funct. Mater. 21 (2011) 810–833.

[12] Z. Hu, M.P. Srinivasan, Y. Ni, Preparation of mesoporous high-surface-area activated carbon, Adv. Mater. 12 (2000) 62–65.

[13] M. Suleman, Y. Kumar, S.A. Hashmi, Flexible electric double-layer capacitors fabricated with micro-/mesoporous carbon electrodes and plastic crystal incorporated gel polymer electrolytes containing room temperature ionic liquids, J. Solid State Electrochem. 19 (2015) 1347–1357.

[14] M.R. Jisha, Y.J. Hwang, J.S. Shin, K.S. Nahm, T.P. Kumar, K. Karthikeyan, N. Dhanikaivelu, D. Kalpana, N.G. Renganathan, A.M. Stephan, Electrochemical characterization of supercapacitors based on carbons derived from coffee shells, Mater. Chem. Phys. 115 (2009) 33–39.

[15] F.R. Bevia, D.P. Rico, A.F. Marcilla Gomis, Activated carbon from almond shells. Chemical activation. 1. Activating reagent selection and variables influence, Ind. Eng. Chem. Prod. Res. Dev. 23 (1984) 266–269.

[16] C. Peng, X. Yan, R. Wang, J. Lang, Y. Ou, Q. Xue, Promising activated carbons derived from waste tea-leaves and their application in high performance supercapacitors electrodes, Electrochim. Acta 87 (2013) 401–408.

[17] M.C. Liu, L.B. Kong, P. Zhang, Y.C. Luo, L. Kang, Porous wood carbon monolith for high-performance supercapacitors, Electrochim. Acta 60 (2012) 443–448.

[18] M.B. Wu, R.C. Li, X.J. He, H.B. Zhang, W.B. Sui, M.H. Tan, Microwave-assisted preparation of peanut shell-based activated carbons and their use in electrochemical capacitors, N. Carbon Mater. 30 (2015) 86–91.

[19] W. Lv, F. Wen, J. Xiang, J. Zhao, L. Li, L. Wang, Y. Tian, Peanut shell derived hard carbon as ultralong cycling anodes for lithium and sodium batteries, Electrochim. Acta 176 (2015) 533–541.

[20] S. Wang, G. Dai, H. Yang, Z. Luo, Lignocellulosic biomass pyrolysis mechanism: a state-of-the-art review, Prog. Energ. Combust. 62 (2017) 33–86.

[21] P.L. Rivilli, R. Alarcón, G.L. Isasmendi, J.D. Pérez, Stepwise isothermal fast pyrolysis (SIFP). Part II. SIFP of peanut shells-Antifungal properties of phenolic fractions, BioResources 7 (2011) 0112–0117.

[22] F. aura-Calixto, J. Cañellas, J. Garcia-Raso, Determination of hemicellulose, cellulose and lignin contents of dietary fibre and crude fibre of several seed hulls, Data comparison, Z. Lebensm. Unters. Forsch. 177 (1983) 200–202.

[23] O. Barbieri, M. Hahn, A. Herzog, R. Kötz, Capacitance limits of high surface area activated carbons for double layer capacitors, Carbon 43 (2005) 1303–1310.

[24] D. Qu, Studies of the activated carbons used in double-layer supercapacitors, J. Power Sources 109 (2002) 403–411.

[25] Y.J. Kim, Y. Horie, S. Ozaki, Y. Matsuzawa, H. Suezaki, C. Kim, N. Miyashita, M. Endo, Correlation between the pore and solvated ion size on capacitance uptake of PVDC-based carbons, Carbon 42 (2004) 491–500.

[26] A. Omri, M. Benzina, N. Ammar, Preparation, modification and industrial application of activated carbon from almond shell, J. Ind. Eng. Chem. 19 (2013) 2092–2099.

[27] A. Satlewal, R. Agrawal, S. Bhagia, P. Das, A.J. Ragauskas, Rice straw as a feedstock for biofuels: availability, recalcitrance, and chemical properties, Biofuel, Bioprod. Bior. 12 (2018) 83–107.

[28] M.K. Singh, Y. Kumar, S.A. Hashmi, Bucky gel of multiwalled carbon nanotubes as electrodes for high performance, flexible electric double layer capacitors, Nanotechnology 24 (2013) 465704.

[29] Y. Kumar, G.P. Pandey, S.A. Hashmi, Gel polymer electrolyte based electrical double layer capacitors: comparative study with multiwalled carbon nanotubes and activated carbon electrodes, J. Phys. Chem. C 116 (2012) 26118–26127.

[30] G.P. Pandey, S.A. Hashmi, Solid-state supercapacitors with ionic liquid based gel polymer electrolyte: effect of lithium salt addition, J. Power Sources 243 (2013) 211–218.

[31] G.P. Pandey, S.A. Hashmi, Y. Kumar, Multiwalled carbon nanotube electrodes for electrical double layer capacitors with ionic liquid based gel polymer electrolytes, J. Electrochem. Soc. 157 (2010) A105–A114.

[32] G.P. Pandey, S.A. Hashmi, Y. Kumar, Performance studies of activated charcoal based electrical double layer capacitors with ionic liquid gel polymer electrolytes, Energy Fuel. 24 (2010) 6644–6652.

[33] J. Ding, H. Wang, Z. Li, K. Cui, D. Karpuzov, X. Tan, A. Kohandehghan, D. Mitlin, Peanut shell hybrid sodium ion capacitor with extreme energy–power rivals lithium ion capacitors, Energy Environ. Sci. 8 (2015) 941–955.

[34] G.P. Pandey, S.A. Hashmi, Experimental investigations of an ionic-liquid-based magnesium ion conducting polymer gel electrolyte, J. Power Sources 187 (2009)

627–634.

[35] M.K. Singh, S.A. Hashmi, Performance of solid-state hybrid supercapacitor with LiFePO$_4$/AC composite cathode and Li4Ti$_5$O$_{12}$ as anode, Ionics 23 (2017) 2931–2942.

[36] Y. Abu-Lebdeh, P.J. Alarco, M. Armand, Single-phased organic plastic crystal electrolytes, J. New Mat. Elect. Syst. 7 (2004) 29–32.

[37] P.L. Arnold, I.J. Casely, Z.R. Turner, R. Bellabarba, R.B. Tooze, Magnesium and zinc complexes of functionalised, saturated N-heterocyclic carbene ligands: carbene lability and functionalisation, and lactide polymerisation catalysis, Dalton Trans. 35 (2009) 7236–7247.

[38] G. Ma, D. Guo, K. Sun, H. Peng, Q. Yang, X. Zhou, X. Zhao, Z. Lei, Cotton-based porous activated carbon with a large specific surface area as an electrode material for high-performance supercapacitors, RSC Adv. 5 (2015) 64704–64710.

[39] K.S.W. Sing, D.H. Everett, R.A.W. Haul, L. Moscou, R.A. Pierotti, J. Rouquerol, T. Siemieniewska, Reporting physisorption data for gas/solid systems with special reference to the determination of surface area and porosity, Pure Appl. Chem. 57 (1985) 603–619.

[40] R. Wang, P. Wang, X. Yan, J. Lang, C. Peng, Q. Xue, Promising porous carbon derived from celtuce leaves with outstanding supercapacitance and CO$_2$ capture performance, ACS Appl. Mater. Interfaces 4 (2012) 5800–5806.

[41] A. Galarneau, F. Villemot, J. Rodriguez, F. Fajula, B. Coasne, Validity of the t-plot method to assess microporosity in hierarchical micro/mesoporous materials, Langmuir 30 (2014) 13266–13274.

[42] T. Kleinert, K. Tayenthal, Separation of cellulose and incrusting substances, Zeitschrift für Angewandte Chemie 44 (1931) 788–791.

[43] T.N. Kleinert, Organosolvent pulping with aqueous alcohol, TAPPI (Tech. Assoc. Pulp Pap. Ind.) 57 (1974) 99–102.

[44] A.F. Pisarnitskii, T.Y. Rubeniya, A.O. Rutitskii, Oak wood hemicelluloses extracted with aqueous-alcoholic media, Appl. Biochem. Microbiol. 42 (2006) 514–518.

[45] A. Yoshida, Y. Kaburagi, Y. Hishiyama, Full width at half maximum intensity of G band in first order Raman spectrum of carbon material as a parameter for graphitization-a study with pyrolytic carbons, Tanso 221 (2006) 2–7.

[46] A.C. Ferrari, D.M. Basko, Raman spectroscopy as a versatile tool for studying the properties of graphene, Nat. Nanotechnol. 8 (2013) 235.

[47] A.C. Ferrari, J. Robertson, Interpretation of Raman spectra of disordered and amorphous carbon, Phys. Rev. B 61 (2000) 14095.

[48] C.Y. Su, Y. Xu, W. Zhang, J. Zhao, X. Tang, C.H. Tsai, L.J. Li, Electrical and spectroscopic characterizations of ultra-large reduced graphene oxide monolayers, Chem. Mater. 21 (2009) 5674–5680.

[49] B. Fang, L. Binder, A novel carbon electrode material for highly improved EDLC performance, J. Phys. Chem. B 110 (2006) 7877–7882.

[50] G. Ren, S. Li, Z.X. Fan, M.N.F. Hoque, Z. Fan, Ultrahigh-rate supercapacitors with large capacitance based on edge oriented graphene coated carbonized cellulous paper as flexible freestanding electrodes, J. Power Sources 325 (2016) 152–160.

[51] G. Ren, X. Pan, S. Bayne, Z. Fan, Kilohertz ultrafast electrochemical supercapacitors based on perpendicularly-oriented graphene grown inside of nickel foam, Carbon 71 (2014) 94–101.

[52] P.Z. Guo, Q.Q. Ji, L.L. Zhang, S.Y. Zhao, X.S. Zhao, Preparation and characterization of peanut shell-based microporous carbons as electrode materials for supercapacitors, Acta Phys. - Chim. Sin. 27 (2011) 2836–2840.

[53] M.C. Liu, L.B. Kong, C. Lu, X.M. Li, Y.C. Luo, L. Kang, Waste paper based activated carbon monolith as electrode materials for high performance electric double-layer capacitors, RSC Adv. 2 (2012) 1890–1896.

[54] A. Jain, S.K. Tripathi, Almond shell-based activated nanoporous carbon electrode for EDLCs, Ionics 21 (2015) 1391–1398.

[55] T.E. Rufford, D. Hulicova-Jurcakova, E. Fiset, Z. Zhu, G.Q. Lu, Double-layer capacitance of waste coffee ground activated carbons in an organic electrolyte, Electrochem. Commun. 11 (2009) 974–977.

[56] T.E. Rufford, D. Hulicova-Jurcakova, Z. Zhu, G.Q. Lu, Nanoporous carbon electrode from waste coffee beans for high performance supercapacitors, Electrochem. Commun. 10 (2008) 1594–1597.

[57] Y. Guo, J. Qi, Y. Jiang, S. Yang, Z. Wang, H. Xu, Performance of electrical double layer capacitors with porous carbons derived from rice husk, Mater. Chem. Phys. 80 (2003) 704–709.

[58] J. Yang, Y. Liu, X. Chen, Z. Hu, G. Zhao, Carbon electrode material with high densities of energy and power, Acta Phys. - Chim. Sin. 24 (2008) 13–19.

[59] X. Li, W. Xing, S. Zhuo, J. Zhou, F. Li, S.Z. Qiao, G.Q. Lu, Preparation of capacitor's electrode from sunflower seed shell, Bioresour. Technol. 102 (2011) 1118–1123.

[60] F.C. Wu, R.L. Tseng, C.C. Hu, C.C. Wang, Effects of pore structure and electrolyte on the capacitive characteristics of steam-and KOH-activated carbons for supercapacitors, J. Power Sources 144 (2005) 302–309.

[61] C.C. Hu, C.C. Wang, F.C. Wu, R.L. Tseng, Characterization of pistachio shell-derived carbons activated by a combination of KOH and CO$_2$ for electric double-layer capacitors, Electrochim. Acta 52 (2007) 2498–2505.

[62] M. Olivares-Marín, J.A. Fernández, M.J. Lázaro, C. Fernández-González, A. Macías-García, V. Gómez-Serrano, T.A. Centeno, Cherry stones as precursor of activated carbons for supercapacitors, Mater. Chem. Phys. 114 (2009) 323–327.

[63] V. Subramanian, C. Luo, A.M. Stephan, K.S. Nahm, S. Thomas, B. Wei, Supercapacitors from activated carbon derived from banana fibers, J. Phys. Chem. C 111 (2007) 7527–7531.

[64] S. Zhao, C.Y. Wang, M.M. Chen, J. Wang, Z.Q. Shi, Potato starch-based activated carbon spheres as electrode material for electrochemical capacitor, J. Phys. Chem. Solid. 70 (2009) 1256–1260.

[65] X. He, P. Ling, J. Qiu, M. Yu, X. Zhang, C. Yu, M. Zheng, Efficient preparation of biomass-based mesoporous carbons for supercapacitors with both high energy density and high power density, J. Power Sources 240 (2013) 109–113.

[66] X. Wei, S. Wan, X. Jiang, Z. Wang, S. Gao, Peanut-shell-like porous carbon from nitrogen-containing poly-N-phenylethanolamine for high-performance supercapacitor, ACS Appl. Mater. Interfaces 7 (2015) 22238–22245.

[67] T. Purkait, G. Singh, M. Singh, D. Kumar, R.S. Dey, Large area few-layer graphene with scalable preparation from waste biomass for high-performance supercapacitor, Sci. Rep. 7 (2017) 15239.

[68] J.R. Miller, Pulse power performance of electrochemical capacitors: technical status of present commercial devices, Proc. 8th International Seminar on Double Layer Capacitors and Similar Energy Storage Devices, Deerfield Beach Fla, Dec. 7-9, 1998.

[69] F. Lufrano, P. Staiti, M. Minutoli, Evaluation of nafion based double layer capacitors by electrochemical impedance spectroscopy, J. Power Sources 124 (2003) 314–320.

[70] P.L. Taberna, P. Simon, J.F. Fauvarque, Electrochemical characteristics and impedance spectroscopy studies of carbon-carbon supercapacitors, J. Electrochem. Soc. 150 (2003) A292–A300.

[71] A. Oz, S. Hershkovitz, N. Belman, E. Tal-Gutelmacher, Y. Tsur, Analysis of impedance spectroscopy of aqueous supercapacitors by evolutionary programming: finding DFRT from complex capacitance, Solid State Ionics 288 (2016) 311–314.

[72] W. Zhang, M. Zhao, R. Liu, X. Wang, H. Lin, Hierarchical porous carbon derived from lignin for high performance supercapacitor, Colloid. Surface. Physicochem. Eng. Aspect. 484 (2015) 518–527.

[73] G.P. Pandey, T. Liu, C. Hancock, Y. Li, X.S. Sun, J. Li, Thermostable gel polymer electrolyte based on succinonitrile and ionic liquid for high-performance solid-state supercapacitors, J. Power Sources 328 (2016) 510–519.

[74] W. Zhang, H. Lin, Z. Lin, J. Yin, H. Lu, D. Liu, M. Zhao, 3 D hierarchical porous carbon for supercapacitors prepared from lignin through a facile template free method, Chem Sus Chem 8 (2015) 2114–2122.

[75] W. Lu, K. Henry, C. Turchi, J. Pellegrino, Incorporating ionic liquid electrolytes into polymer gels for solid-state ultracapacitors, J. Electrochem. Soc. 155 (2008) A361–A367.

[76] C.C. Yang, S.T. Hsu, W.C. Chien, All solid-state electric double-layer capacitors based on alkaline polyvinyl alcohol polymer electrolytes, J. Power Sources 152 (2005) 303–310.

[77] R. Muchakayala, S. Song, J. Wang, Y. Fan, M. Bengeppagari, J. Chen, M. Tan, Development and supercapacitor application of ionic liquid-incorporated gel polymer electrolyte films, J. Ind. Eng. Chem. 59 (2017) 79–89.

[78] V. Chaudoy, F.T. Van, M. Deschamps, F. Ghamouss, Ionic liquids in a poly ethylene oxide cross-linked gel polymer as an electrolyte for electrical double layer capacitor, J. Power Sources 342 (2017) 872–878.

[79] N. Yadav, K. Mishra, S.A. Hashmi, Optimization of porous polymer electrolyte for quasi-solid-state electrical double layer supercapacitor, Electrochim. Acta 235 (2017) 570–582.

[80] Y. Cai, Y. Luo, H. Dong, X. Zhao, Y. Xiao, Y. Liang, M. Zheng, Hierarchically porous carbon nanosheets derived from Moringa oleifera stems as electrode material for high-performance electric double-layer capacitors, J. Power Sources 353 (2017) 260–269.

[81] L. Peng, Y. Liang, H. Dong, H. Hu, X. Zhao, Y. Cai, M. Zheng, Super-hierarchical porous carbons derived from mixed biomass wastes by a stepwise removal strategy for high-performance supercapacitors, J. Power Sources 377 (2018) 151–160.

[82] A. Laheäär, P. Przygocki, Q. Abbas, F. Béguin, Appropriate methods for evaluating the efficiency and capacitive behavior of different types of supercapacitors, Electrochem. Commun. 60 (2015) 21–25.

[83] A.A. Łatoszyńska, P.L. Taberna, P. Simon, W. Wieczorek, Proton conducting gel polymer electrolytes for supercapacitor applications, Electrochim. Acta 242 (2017) 31–37.

[84] L. Nègre, B. Daffos, V. Turq, P.L. Taberna, P. Simon, Ionogel-based solid-state supercapacitor operating over a wide range of temperature, Electrochim. Acta 206 (2016) 490–495.